

Feature extraction for hyperspectral mineral domain mapping: A test of conventional and innovative methods

Lorenz, S.; Ghamisi, P.; Kirsch, M.; Jackisch, R.; Rasti, B.; Gloaguen, R.;

Originally published:

October 2020

Remote Sensing of Environment 252(2021), 112129

DOI: <https://doi.org/10.1016/j.rse.2020.112129>

Perma-Link to Publication Repository of HZDR:

<https://www.hzdr.de/publications/Publ-31596>

Release of the secondary publication
on the basis of the German Copyright Law § 38 Section 4.

CC BY-NC-ND

Feature extraction for hyperspectral mineral domain mapping: A test of conventional and innovative methods

Sandra Lorenz*, Pedram Ghamisi, Moritz Kirsch, Robert Jackisch, Behnood Rasti, Richard Gloaguen

*Helmholtz Institute Freiberg for Resource Technology, Helmholtz-Zentrum Dresden-Rossendorf, Chemnitz
Straße 40, 09599 Freiberg, Germany*

**s.lorenz@hzdr.de | +49 (0) 351 260-4487*

Abstract: Hyperspectral (HS) imaging holds great potential for the mapping of geological targets. Innovative acquisition modes such as drone-borne or terrestrial remote sensing open up new scales and angles of observation, which allow to analyze small-scale, vertical, or difficult-to-access outcrops. A variety of available sensors operating in different spectral ranges can provide information about the abundance and spatial location of various geologic materials. However geological outcrops are inherently uneven and spectrally heterogeneous, may be covered by dust, lichen or weathering crusts, or contain spectrally indistinct objects, which is why classifications or domain mapping approaches are often used in geoscientific and mineral exploration applications as a means to discriminate mineral associations (e.g. ore or alteration zones) based on overall variations in HS data. Feature extraction (FE) algorithms are prominently used as a preparatory step to identify the first order variations within the data and, simultaneously, reduce noise and data dimensionality. The most established FE algorithms in geosciences are, by far, Principal Component Analysis (PCA) and Minimum Noise Fraction (MNF). Major progress has been conducted in the image processing community within the last decades, yielding innovative FE methods that incorporate spatial information for smoother and more accurate classification results. In this paper, we test the applicability of conventional (PCA, MNF) and innovative FE techniques (OTVCA: Orthogonal total variation component analysis and WSRRR: Wavelet-based sparse reduced-rank regression) on three case studies from geological HS mapping campaigns, including drone-borne mineral exploration, terrestrial paleoseismic outcrop scanning and thermal HS lithological mapping. This allows us to explore the performance of different FE approaches on complex geological data with sparse or partly inaccurate validation data. For all case studies, we demonstrate advantages of innovative FE algorithms in terms of classification accuracy and geological interpretability.

We promote the use of advanced image processing methods for applications in geoscience and mineral exploration as a tool to support geological mapping activities.

Keywords: feature extraction, domain mapping, mineral exploration, image processing, hyperspectral imaging, classification

1. Introduction

A main application of spectral imaging in geosciences and mineral exploration is the discrimination of mineralogical or lithological domains, i.e. mixed material classes that are defined based on their relevance for the respective objective, such as distinctive ore or alteration zones. Domain mapping may correspond to a classification of overall data characteristics in the spatial and spectral domain. This approach differs from traditional mineral mapping, which uses the abundance of single minerals or compounds based on specific spectral characteristics.

Domain or class mapping is a well-established remote sensing method and numerous approaches exist (Lu and Weng, 2007; Li et al., 2014; Benediktsson & Ghamisi, 2015), each tailored to the data type and objective of the study. The classification of spectral image data has a number of challenges such as high data dimensionality at a high redundancy, which leads to both memory and time intensive processing as well as the “curse of dimensionality” (Hughes, 1968). The latter describes the phenomenon of declining classification accuracies with rising data dimensionality at constant number of classes and training data (Hughes, 1968).

Feature extraction (FE) methods are a common approach to tackle these challenges (Jia et al., 2013; Benediktsson & Ghamisi, 2015). By projecting the data into a lower dimensional feature space and selecting the most meaningful data features, the data size, dimensionality and redundancy can be reduced dramatically, while most of the informative value is preserved. The extraction of appropriate features is key for a successful subsequent classification, as it determines the amount and relevance of information preserved and passed to the classifier. The most traditional FE approaches such as principal component analysis (PCA) and minimum

noise fraction (MNF), first introduced by Pearson (1901) and Green et al. (1988), respectively, are based on the extraction of orthogonal features. These well-established approaches, however, only consider the input spectral information (e.g., reflectance information) and disregard the valuable spatial information of neighboring pixels, which, if included, can significantly improve the mapping abilities of machine learning algorithms (Ghamisi et al., 2018; Fauvel et al., 2013). Respective advanced algorithms that are able to model both spectral and spatial information simultaneously (“spatially constrained” methods) have been developed over time and have outperformed classical FE approaches in terms of resulting classification accuracy using standard test datasets (Rasti et al., 2014; Rasti et al., 2016; Rasti & Gudmundsson, 2016). Such datasets commonly represent well validated land cover or urban scenes with rather distinct and homogeneous classes; thus, contrasting typical geoscience scenery. These algorithms incorporate spatial information either via a penalty term augmented to the fidelity term of a cost function or solve the problem subject to a constrain. In Rasti et al. (2016) and Rasti et al. (2014), two spatially constrained FE approaches, orthogonal total variation component analysis (OTVCA) and wavelet-based sparse reduced-rank regression (WSRRR), were proposed and used, respectively, and their performances were evaluated for land cover classification. The former one incorporates the spatial information via total variation penalty and the latter one includes spatial information by applying ℓ_1 penalty on the wavelet coefficients. The obtained results in those previous studies also demonstrate that OTVCA and WSRRR improved the performance of conventional feature extraction approaches in terms of classification accuracies for land cover classification in both rural and urban areas.

The presented study aims to showcase the potential of advanced FE for domain mapping in geoscientific and economic geology applications. Using three case studies, we compare the performance of two conventional (PCA, MNF) and two advanced spatially constrained FE algorithms (OTVCA, Rasti et al. (2016): Orthogonal total variation component analysis, WSRRR, Rasti et al. (2014): Wavelet-based sparse reduced-rank regression). A supervised support vector machine (SVM) classification is performed on each dataset to evaluate the quality and relevance of the extracted features in terms of classification accuracy and

geological meaningfulness. The case studies include real and representative applications of remote sensing in geosciences that cover different challenges with regard to target characteristics, platform and sensor, i.e. including (1) drone-borne data from a lightweight, low signal-to-noise ratio (SNR) sensor in the visible and near infrared (VNIR) range, (2) terrestrial small-angle (non-nadir) data from a sensor operating in the VNIR to short-wave infrared (SWIR) range, (3) terrestrial small-angle data in the long-wave infrared (LWIR) range providing spectrally highly mixed signatures. In all three examples, the provided training data is extremely limited and the domains of interest are spectrally indistinct, which is typical for geological targets.

2. Methodology

2.1 General workflow

Figure 1 depicts a generalized overview on the used processing workflow.

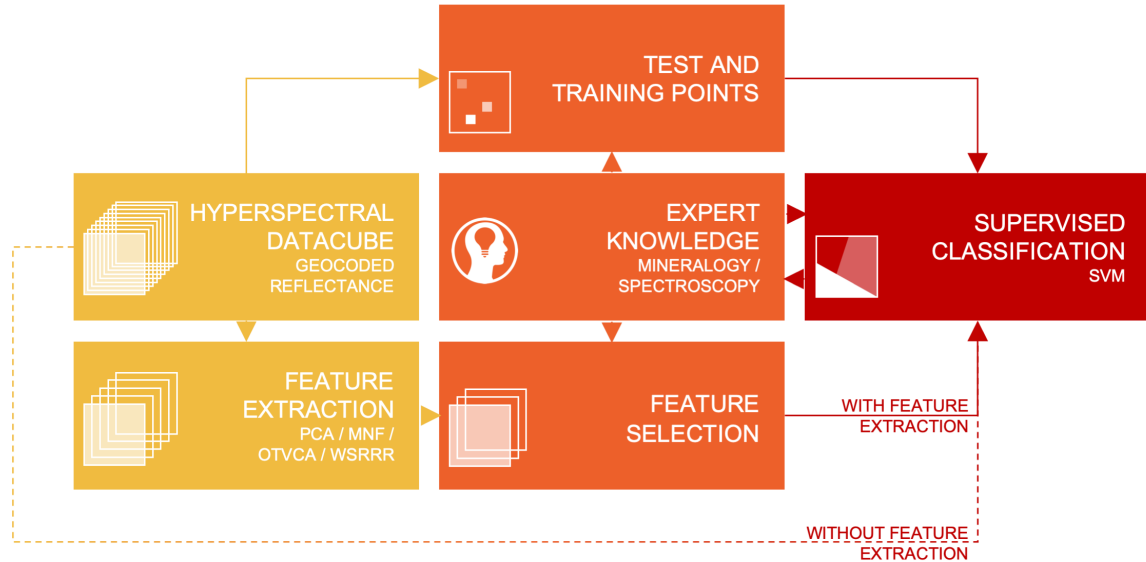


Figure 1. General workflow of hyperspectral data classification with and without prior application of feature extraction methods.

In preparation, each case dataset was fully corrected for spectral and spatial rightness according to its sensor- and platform specific workflow (compare Jakob et al., 2017; Lorenz et

al., 2018a). Pixels unrelated to the geological target of the case study (e.g., calibration panels, sky, vegetation) were masked prior to further processing.

A set of established (PCA, MNF) and innovative (OTVCA, WSRRR) FE algorithms was applied separately on each dataset using the same number of output features within each case study. The processing time was determined under equal computational prerequisites for each run. All the methods investigated in this paper are implemented in Matlab on a computer having Intel(R) Core(TM) i7-6700 processor (3.40 GHz), 32 GB of memory and 64-bit Operating System. Within each case study, an equal number of features was selected from each FE result. The feature subsets were defined by manually choosing image features with a geological meaning while rejecting features dominated by noise or illumination differences. For each case study, the feature subsets were used as an input for an SVM classification to discriminate geological domains of interest and provide a basis for a comparison of the FE approaches regarding their geoscientific value. The training data corresponds to regions of interest that were defined based on geological validation from field observations, samples and spectral reference measurements. An additional classification on the full, original dataset was performed for each case study to compare the classification performance of features vs. full data dimensionality. The accuracy of each classification result was estimated using three established accuracy measures: average accuracy (AA), overall accuracy (OA) and kappa coefficient (k).

The tested FE algorithms as well as the used classifier are introduced in the following.

2.2 Algorithms used

Principal component analysis (PCA) aims at transforming the input hyperspectral data into a lower dimensional subspace using a linear transformation approach which maximizes the signal variance (Jolliffe, 2002). PCA reduces the dimensionality of hyperspectral datasets with interrelated variables, while it retains most of the variation in the dataset. The output of PCA is a set of features, also known as principal components (PCs), which are orthogonal to each other and are ordered in such a fashion that the first PC corresponds to the greatest variance,

the second component corresponds to the second greatest variance and so on. Therefore, the first few principal components which capture the major variance of the data can be a representative for the higher dimensional data.

Minimum noise fraction (MNF), which was specifically proposed to analyze remotely-sensed hyperspectral and multispectral images, computes the normalized linear combinations of the original bands which maximize the SNR by minimizing the variance of the noise with respect to the variance of the signal, and therefore, maximize the quality of the input hyperspectral data (Green et al., 1988). In a similar manner to PCA, MNF produces orthogonal features ordered by their information content in which the first few components contain very high SNR. While PCA searches for an orthogonal subspace to capture the maximum variance of the data, MNF seeks a subspace to maximize the signal to noise ratio, making it more suitable for data restoration and data quality improvement.

Orthogonal total variation component analysis (OTVCA) was recently introduced in Rasti et al. (2016) by developing a non-convex optimization technique and a low-rank (subspace) model. It extracts the most informative features from the observed data (F). OTVCA estimates the reduced features by solving the following constraint cost function problem:

$$(\hat{\mathbf{A}}, \hat{\mathbf{V}}) = \arg \min_{\mathbf{A}, \mathbf{V}} \frac{1}{2} \|\mathbf{F} - \mathbf{A}\mathbf{V}^T\|_F^2 + \lambda \sum_{i=1}^r \left\| \sqrt{(\mathbf{D}_h \mathbf{a}_{(i)})^2 + (\mathbf{D}_v \mathbf{a}_{(i)})^2} \right\|_1 \quad \text{s.t. } \mathbf{V}^T \mathbf{V} = \mathbf{I}_r, \quad (1)$$

where \mathbf{V} contains the low-rank basis, $\|\mathbf{A}\|_{TV}$ is the total variation norm applied spatially (Rasti et al., 2016) and λ is known as the TV tuning parameter which balances the amount of smoothness. We should note that the low-rank features, \mathbf{A} , and the basis matrix (for the subspace), \mathbf{V} , are unknown. Therefore, they both need to be estimated. To solve the aforementioned optimization problem, a cyclic descent (CD) was suggested in Rasti et al. (2016). As can be seen in Eq. (1), the cost function is composed of two terms. The first term, the fidelity term, tries to minimize the difference between \mathbf{F} and the estimated $\mathbf{A}\mathbf{V}^T$. The second term is the regularization term, which models the spatial dependencies using the total variation norm.

Wavelet-based sparse reduced-rank regression (WSRRR) was proposed in Rasti et al. (2014), to represent hyperspectral images using a few informative features automatically. WSRRR uses a sparse and low-rank model to represent the hyperspectral data. In Rasti et al. (2014), the following optimization model is used to estimate W and V , simultaneously:

$$(\hat{W}, \hat{V}) = \arg \min_{W, V} \frac{1}{2} \|F - DWV^T\|_F^2 + \lambda \sum_{i=1}^r \|w_{(i)}\|_1 \text{ s.t. } V^T V = I_r, \quad (2)$$

where D contains the two-dimensional wavelet basis and W contains unknown 2D wavelet coefficients. In order to enforce sparsity into (2), an l_1 penalty on the wavelet coefficients was considered. The promotion of sparsity on the extracted features improves the SNR, which leads to more accurate classification maps. As can be seen in Eq. (2), the cost function consists of two terms. The first term, the fidelity term, tries to minimize the difference between F and the estimated DWV^T . The second term, the regularization term, tries to model spatial dependencies using an l_1 norm applied on wavelet coefficients.

Support vector machines (SVM) classifier is a widely-used technique for the classification of hyperspectral images since it can effectively handle the high dimensionality of hyperspectral images when only a limited number of training samples is available. Based on the studies conducted in Ghamisi et al. (2017), SVM is found to be efficient, stable, and accurate compared to several other machine learning-based classification techniques. There is a large number of scientific papers (such as these two review papers Ghamisi et al. (2017) and Benediktsson & Ghamisi, (2015)) which clearly demonstrate that a joint use of a robust FE technique and the SVM classifier can shape a strong machine learning approach, particularly for the classification of hyperspectral images. SVM tries to define an optimal separating hyperplane, also known here as a classification boundary, within the multidimensional feature space to differentiate between the training samples of two classes of interest. The best hyperplane is the one that leaves the maximum margin from the closest training samples (also known as support vectors) of both classes. The hyperplane is placed in the multidimensional feature space by considering an optimization problem that is solved via structural risk minimization.

The SVM was initially introduced to tackle linear problems, although decision boundaries often need to be nonlinear to address classification problems due to the complex and nonlinear nature of hyperspectral image classification. In such cases, a nonlinear mapping using kernel methods is used to project the data into a high-dimensional feature space where the input nonlinear data are linearly separable. For the current study, we use the Gaussian radial basis function (RBF) kernel, which is the most widely-used kernel for hyperspectral image analysis (Scholkopf & Smola, 2002; Waske et al., 2009). The RBF kernel contains two important parameters, including C (the parameter that controls the amount of penalty during the SVM optimization) and γ (the spread of the RBF kernel), which are automatically traced using a parameter selection method based on cross-validation (Chapelle et al., 2002).

3. Introduction of case studies

3.1 Case study 1: UAS-borne VNIR

The first case study is a drone-borne hyperspectral survey over the Otanmäki mine, located 200 kilometers southeast of Oulu in the center of Finland. The analyzed scene covers parts of the Metsämalmi outcrop, located at the eastern margin of the Otanmäki deposit (Fig. 2a). The site is characterized by Paleoproterozoic gabbro-anorthosites that intruded the Archean granitic gneiss basement. The gabbros host Fe-Ti-V oxide ore bodies, linked to a magnetite-ilmenite mineralization of economic interest (Pääkkönen, 1956; Lindholm et al., 1980; Huhma et al., 2018). Recent geochemical studies attest to the high complexity of the Otanmäki suite in terms of lithology and geometry (Kärenlampi et al., 2019). The ore bodies occur as hundreds of lenses and veins with widths of 3–50 m and lengths up to 200 m (Maier et al., 2015), containing up to 40 wt.% magnetite.

All abundant lithologies, including the ore, lack distinctive absorption features in the examined spectral range. The irregular shape of the ore bodies, their heterogeneous composition and locally dense lichen cover further contribute to create a challenging target for supervised classification methods. For this example, we defined four distinct classes: ore, amphibolite,

anorthosite and leucogabbro (Fig. 3). This distinction is based on a detailed, hand-drawn and subsequently geolocated geologic map made by *Rautaruukki Oy*, which was kindly provided by the *Otanmäki Mine Oy* company.

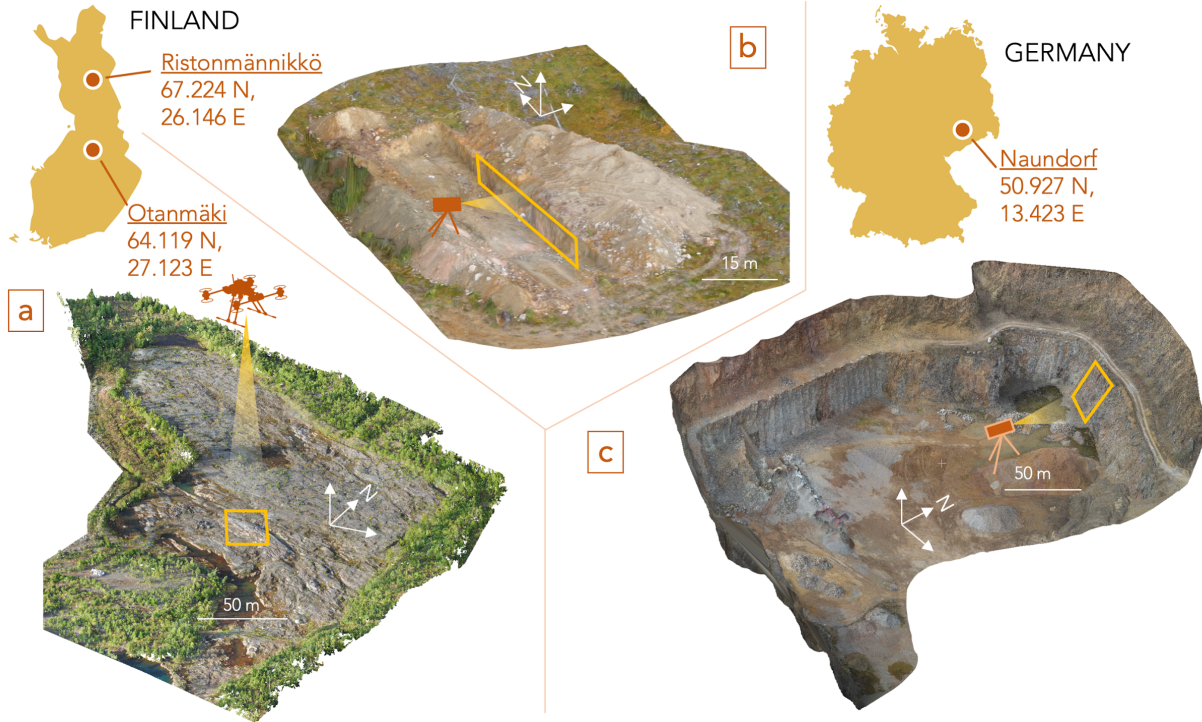


Figure 2. Location of the three study areas as well as coverage of the discussed data sets (indicated by yellow polygons): a) UAS-based VNIR (case study 1), b) terrestrial VNIR-SWIR (case study 2), c) terrestrial LWIR (case study 3)

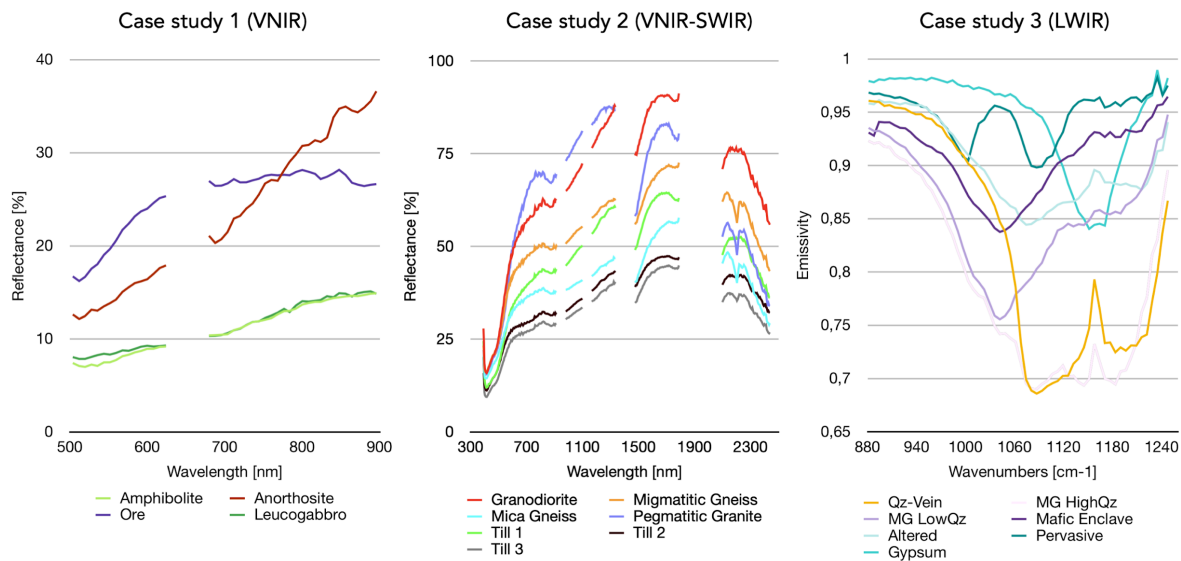


Figure 3. Spectral characteristics of the classes defined for each case study area. The displayed spectra are averages of all pixels used for training of each respective class. Spectral artifacts due to sensor gaps and strong atmosphere-related noise are whitened out for better visibility.

The ore zone extents were mapped based on field observations, drillings, and magnetic susceptibility measurements. Due to potential local positioning inaccuracies, the geological map could not be used directly for the extraction of test and training pixels, but served as a general guideline for class discrimination and visual verification of classification results. The final selection of validation points was supported by geological as well as spectral field observations, and refined based on spectral homogeneity in the hyperspectral image to avoid accidental mislabeling due to shaded or highly inhomogeneous areas. The selected validation points were divided into 60–400 training pixels (average of 200 px) and 90–400 test pixels (average of 200 px) per class. The data set was acquired using a light-weight VNIR hyperspectral imager deployed from a hexacopter drone (for details see Table 1). The detailed acquisition and processing workflow can be found in Jakob et al. (2017) and Jackisch et al. (2019), respectively.

Table 1. Overview on important sensor, target and acquisition parameters for the three case studies.

Case Study	1	2	3
Location	Otanmäki, Finland	Ristonmännikkö, Finland	Naundorf, Germany
Geological target	Fe-Ti-V deposit (scraped outcrop)	Tectonic structures in crystalline basement and sedimentary cover rocks (artificial trench wall)	Hydrothermal alteration zones (quarry face)

Deployed Sensor	Senop Rikola Hyperspectral Imager (504–900 nm, frame based)	Specim AisaFENIX (380–2500 nm, push- broom)	Telops Hyper-Cam LW (7700-11800 nm, frame-based)
Sensor Setup	Drone-based (hexacopter)	Ground-based (tripod)	Ground-based (tripod)
Sensor Orientation	Nadir	Horizontal	Near-horizontal (varying)
Sensor-Target Distance	50 m	13 m	55 m
Data size (columns/ rows/bands)	960/890/50	1389/326/450	667/746/58
Image footprint	ca. 30 m x 27 m	ca. 20 m x 4 m	ca. 15 m x 16 m
Extracted features/ selected features	15/6	20/10	20/12

3.2 Case study 2: terrestrial VNIR-SWIR

The VNIR-SWIR dataset from the Ristonmännikkö site was acquired during a ground-based hyperspectral imaging campaign at a paleoseismic trench dug across a post-glacial fault in the northern Finnish part of the Fennoscandian Shield (Kirsch et al., 2019; Fig. 2b). At this site, neotectonic deformation has produced discrete reverse fault scarps with small offsets within an Archean basement and glacial-cover sediment sequence. Seven lithologic classes were considered for classification, comprising basement units (granodiorite, migmatitic gneiss, mica gneiss, pegmatitic granite) and cover sequences (till 1, 2 and 3). The training data for the supervised classification is based on image spectra at 30 sample locations, labelled according to generalized lithologic descriptions provided by the geologists on site. Laboratory (X-ray diffraction analysis) and in-situ (handheld X-ray fluorescence (XRF) analyzer and VNIR-SWIR

spectrometer) analytical data were used for the validation of the spectral features and to establish a link between lithologic classes and spectral, mineralogical, and chemical composition (Kirsch et al., 2019). In order to increase the number of training pixels per class and to compensate for any georeferencing, registration and sample-localization errors, 24 pixels surrounding each of the original validation points were also included in the training dataset. The selected validation points were divided into 50–175 training pixels (average of 100 px) and 20–35 test pixels (average of 25 px) per class. A non-orthorectified geological map of the outcrop (Ojala et al., 2019) served as a guideline for a visual evaluation of classification results.

Damp, cold and cloudy conditions during image acquisition had a clearly negative effect on the SNR of the hyperspectral data, which is manifested by low reflectance values, strong water absorptions and noisy spectra, particularly in the SWIR range (Fig. 3). This may lead to spectrally indistinctive classes but illustrates an acquisition during operational conditions.

Details on the acquisition and processing workflow can be found in Table 1, as well as in Lorenz et al. (2018a), Kirsch et al. (2018) and Kirsch et al. (2019), respectively.

3.3 Case study 3: terrestrial LWIR

The third case study was performed at the Naundorf quarry in the state of Saxony, Germany (Fig. 2c). It showcases parts of the As-Zn-Cu-In-Ag-bearing polymetallic sulfide vein network characteristic for the Freiberg mining district. In the Naundorf quarry, the faults are associated with phyllic hydrothermal alteration of the late Variscan biotite granite host.

The site has already been investigated using different HS sensors in Kirsch et al. (2018). The long-wave infrared data set was acquired as a mosaic of data frames using a Telops Hyper-Cam LW HS imager (for details see Table 1). The detailed acquisition and processing workflow can be found in Lorenz et al. (2018b) and Kirsch et al. (2018), respectively. According to the mineralogical discrimination of Kirsch et al. (2018), the main lithological classes of the Naundorf quarry are monzogranite, moderately altered and pervasively altered monzogranite, mafic enclaves of quartz-monzonitic composition and quartz veins. For this study, the analyzed

scene was further subdivided, yielding a total of spectrally distinct 7 classes (Fig. 3): Qz-rich zones/veins, monzogranite (high and low quartz), mafic enclaves, moderately altered monzogranite, pervasive alteration, and gypsum. A schematic geological map of the outcrop was used for a general visual evaluation of the classification results. The map is based on field observations in the accessible portion of the outcrop and visual interpretation of an RGB textured digital outcrop model in the inaccessible part of the outcrop. However, due to the inaccessibility of most of the outcrop (in particular the middle and upper part) and the visual similarity of some classes, the map only outlines general expected lithological variations. A detailed discrimination of the hydrothermal alteration zone into gypsum-rich parts and pervasive alteration, the discrimination of monzogranite with differing quartz content or the exact location of all mafic enclaves for the full extent of the study area was not feasible. For this reason, the validation map does only include generalized lithological classes. Validation points for training and test data were therefore selected manually based on the available accurately geolocated geological as well as spectral field observations, and refined according to spectral homogeneity in the hyperspectral image to avoid mislabeling in shaded or inhomogeneous areas. The selected validation points were divided into 20–80 training pixels (average of 37 px) and 60–300 test pixels (average of 155 px) per class.

4. Results

4.1 General performance of the tested FE methods

A comparison of the geologically most relevant feature bands per tested FE algorithm (shown exemplary for the first case study in Fig. 4) reveals similar content and quality in the first two or three bands for all tested FE methods. In successive bands, major differences arise.

The most obvious trend is the overall more smooth and coherent appearance of the feature bands extracted by the spatially constrained methods OTVCA and WSRRR, with an apparent increase in spatial smoothing towards higher feature numbers. This effect is stronger for OTVCA and leads to the manifestation of large-scale blurry structures in feature bands of

300 higher index. In contrast, the traditional methods PCA and MNF yield much noisier, but also
301 more detailed feature bands with consistent spatial resolution/scale throughout all feature
302 bands. However, apart from the very first feature bands, extracted geology-relevant features
303 additionally highlight noise and image artifacts that overprint the relevant information. In the
304 depicted UAV-borne case study 1, these artifacts comprise mostly illumination differences
305 between individual images of the processed mosaic as well as remaining topography-related
306 artifacts. OTVCA and WSRRR seem to suppress this effect and show an overall much better
307 separation of geology-related features and image artifacts, which allows for a much easier
308 manual selection of relevant feature bands with parallel rejection of artifact- or noise-only
309 feature bands.

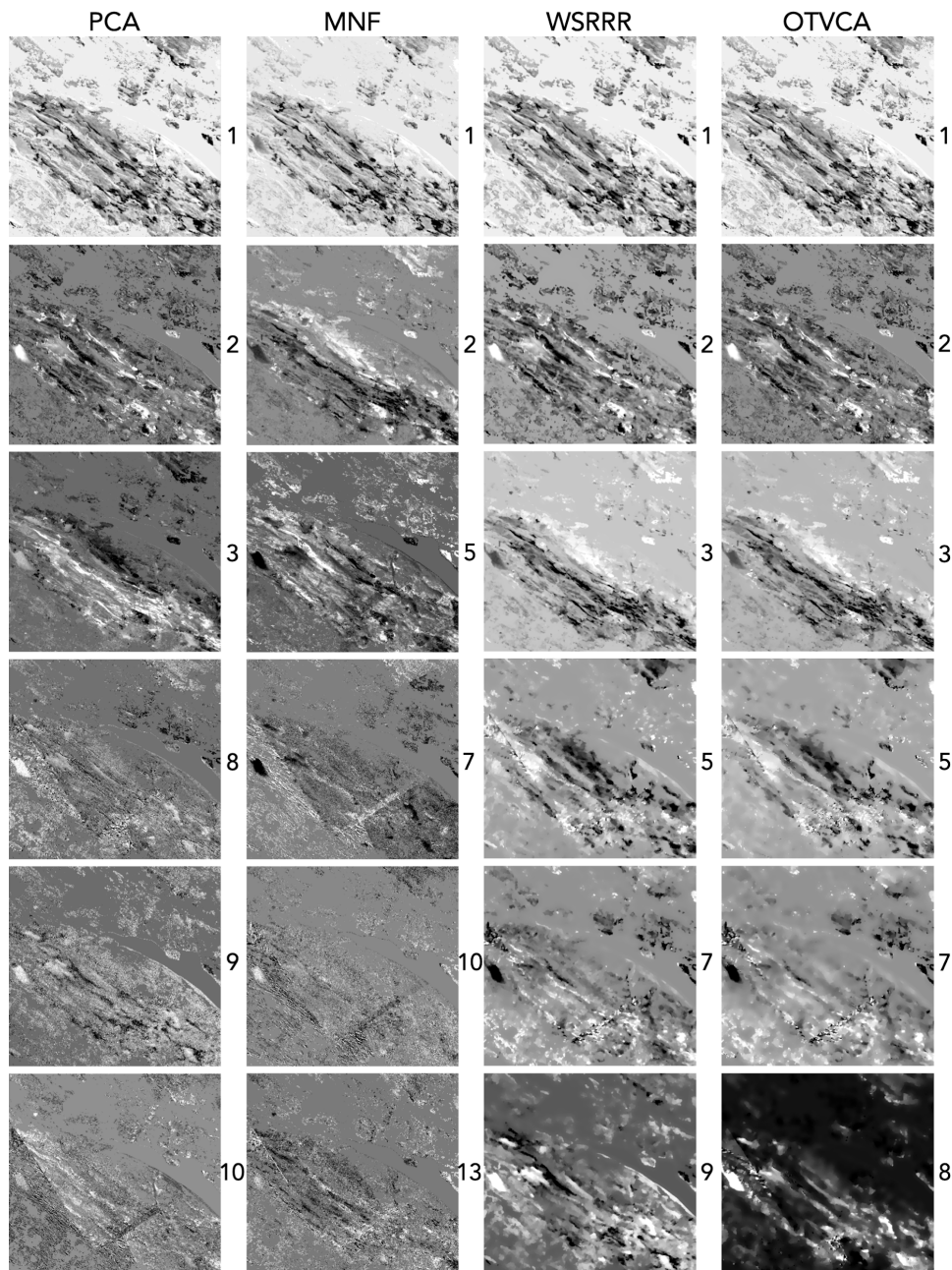


Figure 4. Comparison of the six geologically most relevant feature bands per tested FE algorithm (index indicated by number label), which were selected for subsequent classification (case study: UAS-VNIR).

The analysis of the processing time for feature extraction from each of the dataset shows clear differences in dependence of the algorithm (Fig. 5). The traditional FE methods, PCA and MNF, exhibit extremely short processing times (in average ~2 microseconds/pixel for PCA and ~30 microseconds/pixel for MNF), while the innovative FE methods require longer processing times

(in average ~0.3 milliseconds/pixel for WSRRR and ~2.1 milliseconds/pixel for OTVCA). In particular OTVCA is very computing-intensive (about 1000 times slower than PCA). The trend is consistent for all three case studies.

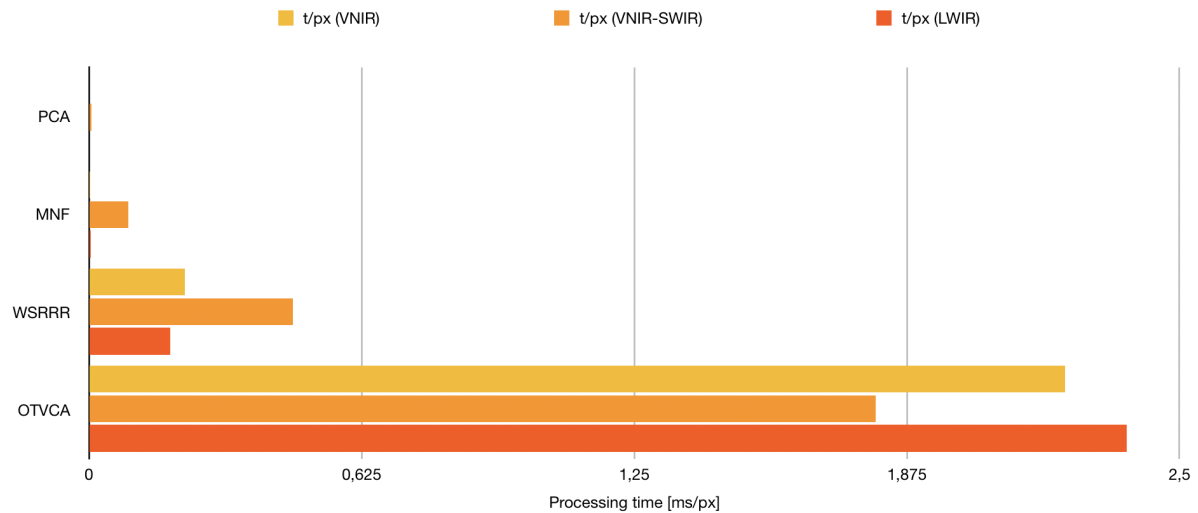


Figure 5. Performance of the tested FE algorithms in regards of processing time (in milliseconds per data pixel) for the extraction of 20 image features per dataset.

In terms of accuracy performance of SVM, the usage of FE prior to SVM is clearly advantageous, as it increases all analyzed accuracy measures (OA, AA, k) by several percent compared to no prior FE (Fig. 6).

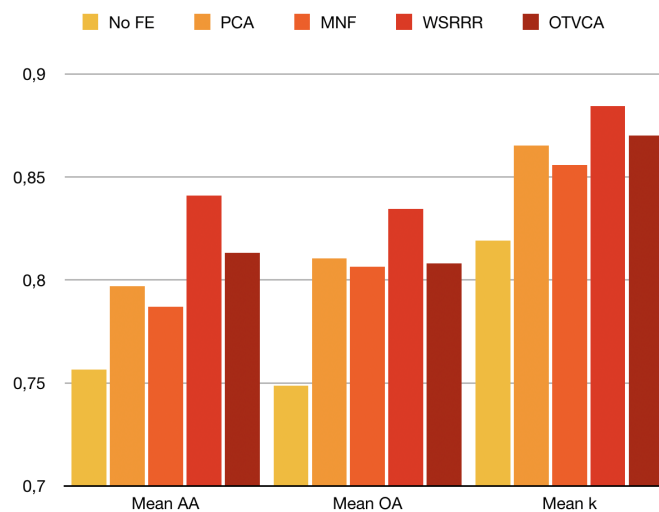


Figure 6. Average performance of SVM classification in terms of accuracy using the tested FE algorithms as well as using no prior FE.

The highest accuracy throughout all categories is accomplished by WSRRR (AA = 84%, OA=83%, k=88%, average of all case studies). Interesting is also the consistently better accuracy performance of PCA in comparison to MNF in all case studies (difference of 0.4-1% for all accuracy measures).

4.2 Classification results VNIR (Otanmäki)

The main host rock types of the Otanmäki site are leucogabbro, amphibolite and anorthosite. In theory, those lithologies are not discriminable in the analyzed part of the electromagnetic spectrum, as their main mineral components, plagioclase and amphibole, are spectrally indistinct in the VNIR. Leucogabbro and amphibolite accordingly show nearly equal spectral signatures in our data (Fig. 3). However, differences in the overall spectral shape of anorthosite and leucogabbro/amphibolite do exist (Fig. 3), which might correspond to alteration of the protolith or minor abundances of spectrally active minerals. The ore zones can be distinguished from non-ore zones based on locally abundant iron oxide absorption features of weathering products of the magnetite/ilmenite mineralization.

In all performed classifications, anorthosite is clearly delineated as linear features following a NW-SE trend (Fig. 7). In contrast, leucogabbro and amphibolite are only separated clearly when using advanced spatially constrained FE methods. Despite their spectral similarity, slight differences in texture and brightness might allow a discrimination based on spatial features. Traditional FE attempts are not able to separate the two classes and show an intermingled and noisy result. The leucogabbro is mapped as a coherent unit in the NE part of the area, which corresponds to the spatial distribution of the unit in the reference geological map. The distribution pattern of the detected ore zones does not completely match those of the geological reference map, but agree largely with the general location and orientation of the mapped units and are coherent in all classification results.

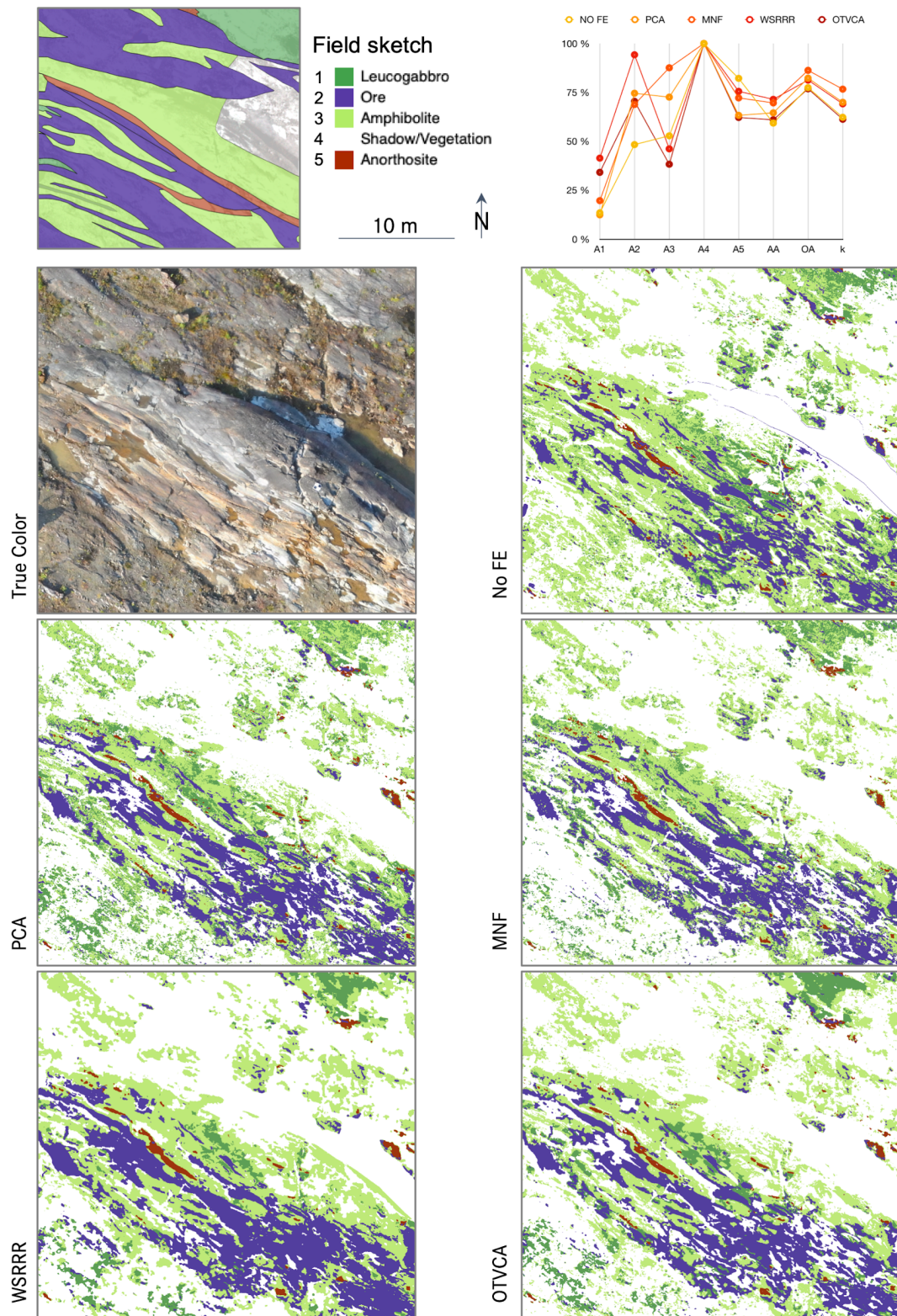
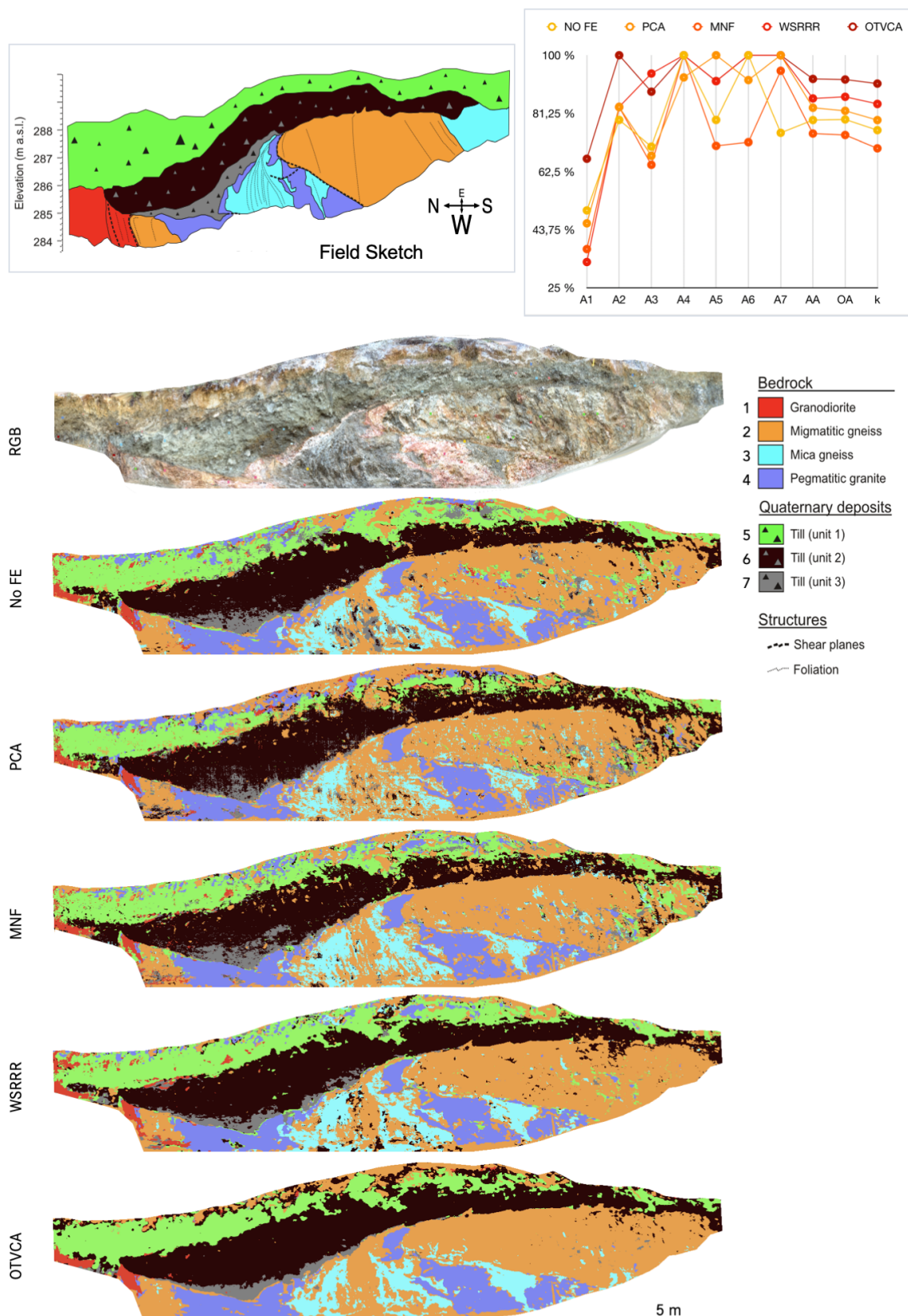


Figure 7. Performance of SVM classification based on different FE approaches for the drone-borne VNIR survey over the Otanmäki ore deposit (Finland). A1-A5 refer to the respective class specific accuracies.

Not only do variable rock compositions inhibit a clearer classification, but the reference geologic map itself is prone to slight shifts in x-y directions. This might be due to inaccurate georeferencing of this map, but also the time difference between the geological mapping and our data acquisition might contribute to inaccuracies in regards of alteration, vegetation and soil coverage. Also, this geologic map was part of a much larger regional geologic mapping, meaning a larger scale was applied to distinguish target rocks at the time. It is unclear how well the drawn boundaries superimpose on the actual rock zones, but a shift of 1-2 m in each direction is likely.

4.3 Classification results VNIR-SWIR (Ristonmännikkö)

In the Ristonmännikkö case study, all methods deliver geologically sensible and interpretable results that to a large extent match the reference geological map (Fig. 8). Discrepancies to the geologic map and the validation data set that result in low classification accuracies (Fig. 8) include (i) the occurrence of migmatitic gneiss within the mica gneiss unit in the center of the outcrop in the classification image, which is mapped as either mica gneiss or pegmatitic granite in the reference map, (ii) the missing occurrence of mica gneiss in the right side of the reference image, (iii) the granodiorite mapped in the far left side of the classification image, which has a smaller spatial extent than the one in the reference map. These differences can be mostly explained by the missing geolocation of the field sketch, which challenges to locate the extent of the mapped lithological boundaries within the classification image. Such, the units on either end of the reference map are possibly only partly covered by the hyperspectral scan. Furthermore, misinterpretation during geological mapping cannot be excluded. There are only subtle differences between the classification results. For instance, the areal extent of till unit 3 differs slightly between the images.



383

384 *Figure 8. Performance of SVM classification based on different FE approaches for the terrestrial VNIR-*

385 *SWIR survey at Ristonmännikö paleoseismic trenches (Finland). A1-A7 refer to the respective class*

386 *specific accuracies.*

The noise level is greatest in the PCA image, followed by the classification image without prior FE, but some of the noise may actually correspond to real features, such as (i) pixels in the till units mapped as either one of the basement units, which may correspond to basement-derived pebbles in the till, and (ii) the pixels mapped as till 3 in any of the basement units (e.g., evident in the WSRRR image) which may be explained by the draping of these units with the friable till material from above.

OTVCA provides the smoothest/cleanest result amongst all trialed classification approaches, the highest accuracy measures for all AA (92%), OA (92 %) and k (91%), and most closely resembles the appearance of a geologic map. However, locally, the uniformity displayed by the OTVCA image may hinder the delineation of faults, which manifest themselves as small-scale, non-continuous, lithologically variable layers (e.g., shear plane in the lower left part of the scene easily identified in the PCA and MNF images).

The suppression of noise may also result in the sharp appearance of transitions between units which may be gradual in reality (e.g. boundary between till units 2 and 3), and the obliteration of textural features, such as interlayering or foliation (compare smoothness of OTVCA with “striped” appearance of MNF in the central portion of the image).

4.4 Classification results LWIR (Naundorf)

All classification results for the Naundorf scene yield geologically plausible results that align well with field observations documented in the geological reference map (Fig. 9). The classification maps show a ubiquitous distribution of low- and high-quartz monzogranite host rocks and clearly defined zones of gypsum and pervasively altered monzogranite spatially limited to the core of the hydrothermal zone. The altered monzogranite is correctly mapped around pervasively altered hydrothermal zones, the mapped mafic enclaves correspond to their true size, shape and (random) distribution in the unaltered host rock.

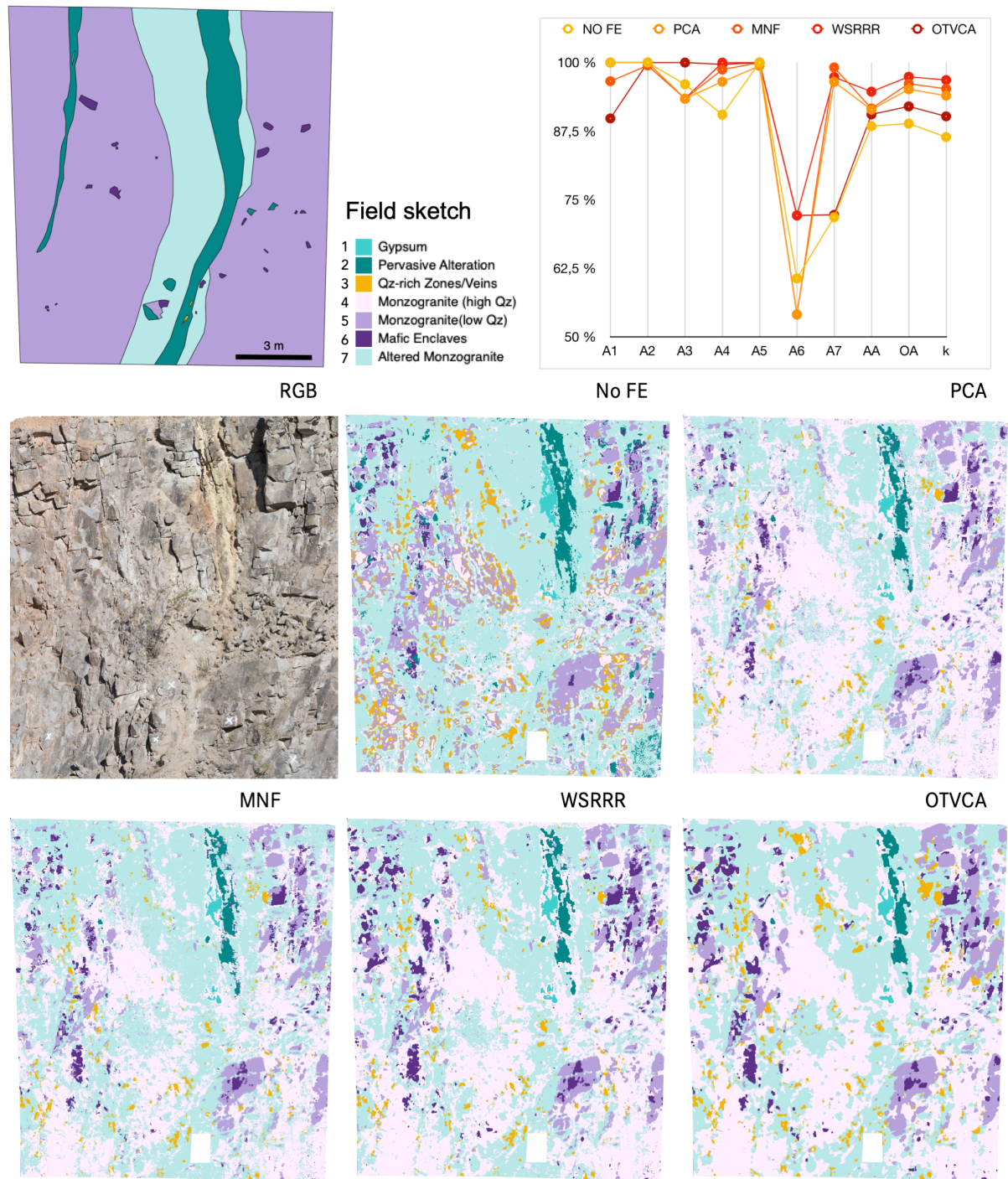


Figure 9. Performance of SVM classification based on different FE approaches for the terrestrial LWIR survey at Naundorf quarry (Germany). A1-A7 refer to the respective class specific accuracies.

The classification with no prior FE has the poorest performance in terms of overall classification accuracy (Fig. 9, AA=88%, OA=89%, k=86% for no FE vs. AA=95%, OA=97%, k=97% for WSRRR). In comparison with the other classification maps, the classification with no prior FE

generally has a noisy appearance showing areas of mixed lithologies and units with highly serrated boundaries. From a geological perspective, the areal extents of mafic enclaves and high-Qz monzogranite appear underestimated, the quartz-rich veins are overestimated, and pervasively altered monzogranite is locally misclassified in areas outside of the hydrothermal zone. Whereas PCA, MNF and WSRRR deliver almost identical results, the OTVCA image is less noisy and generally exhibits pixel groups of larger size. This aggregation leads to a slight overestimation of areal extent of enclaves and other units as well as some geometric distortion and loss of textural details (e.g. the vein-like shape of gypsum in the upper part of the hydrothermal zone).

Particularly low classification accuracies are obtained for the mafic enclave class, which is spectrally very similar to the low-quartz monzogranite. Due to the spectral non-distinctiveness of this class, classifications based on PCA and MNF lead to speckled results that lower the accuracy ($A_6=54\%$), whereas spatially constrained FE methods are able to discriminate this class as small but coherent regions ($A_6=72\%$).

5. Discussion

The results of the study showed a clear trend on the advantageous usage of feature extraction and selection for enhanced lithological classification. Data classification without prior FE showed to return the lowest accuracy of all classification attempts, which supports the theory on the “curse of dimensionality”. Variations of illumination due to shadow and changing weather conditions during data acquisition are particularly problematic when applying classification on datasets without prior FE. Within the classification result these illumination differences can become visible e.g. as sharp and straight class borders, affecting class discrimination. This effect can be substantially reduced by prior FE and the rejection of affected feature bands for classification.

The importance of masking spectrally distinct but geologically irrelevant interfering image parts, such as vegetation or reference targets, prior to FE is apparent. Particularly in cases

where spectral differences between lithologies are subtle, those spectrally highly variant objects would otherwise dominate over geological information in extracted features.

The study further showed clear differences in the performance of conventional and spatially constrained FE approaches. The use of traditional FE algorithms often leads to the discrimination of smaller objects within larger geological domains. The resulting speckled appearance mostly originates in spectrally indistinct classes, low SNR or small-scale illumination variations. Lithological domains, however, aim to be spatially homogeneous, even if of inhomogeneous mineralogical composition. Spatially constrained FE methods (OTVCA and WSRRR) yielded geologically more accurate classification results. The ability for spatial constraining allows to achieve a particularly smooth classification result, while still allowing the detection of small objects. This is especially advantageous for the detection of spatially small objects (e.g. mafic enclaves in the LWIR/Naundorf case study), which otherwise are easily missed due to this “class noise”. On the other hand, smooth classification results by spatially constrained FE methods can also lead to an overestimation in the size of small objects and loss of textural detail, in particular within non-continuous, lithologically variable zones. Classifications based on spatially constrained feature extraction methods, however, are not comparable to a subsequent smoothing of a noisy classification image. Post-processing of the classification result by filtering, smoothing or segmenting often helps to increase the classification accuracy, as separated misclassified pixels are replaced by the surrounding true positives. However, this approach is not able to reconstruct initially false classified areas and can even cause the extrapolation of errors to larger pixel groups. Secondly, very small objects, even if correctly classified, might be removed by the smoothing. Spatially constrained feature extraction methods, in contrast, determine spatially related pixel groups before the classification is performed. The achieved smoothing is therefore solely data-driven. Small classified objects have a much higher probability to be of true nature than in spatially non-constrained FE. This makes spatially constrained feature extraction methods particularly suited for the classification of scenes with high spatial scale variability, for example for the mapping of veins, enclaves or clasts in a larger matrix. Similar to this study, where the performance of

different feature extraction approaches has been evaluated and compared against each other, in Rasti et al. (2016) and Rasti et al. (2014), OTVCA and WSRRR were proposed and used, respectively, and their performances were evaluated for land cover classification. The obtained results in those previous studies also demonstrate that OTVCA and WSRRR improved the performance of conventional feature extraction approaches in terms of classification accuracies for land cover classification in both rural and urban areas.

The consistently better accuracy performance of PCA in comparison to MNF in all case studies can be explained by their respective underlying approach. MNF seeks a projection to minimize the Gaussian noise and cannot take into account other noise types such as stripping, sparse noise, and shot noise. PCA, on the other hand, captures the variance of the dataset regardless of the type of the existing noise. In this context, if the dataset has high SNR, as this is the case for our datasets, PCA can represent the data into a few informative PCs. In the experiments, after performing PCA, we selected only the PCs with high SNR and, therefore, the PCs with lower SNRs which often degrade the classification results have been neglected. This could be the reason why PCA could outperform MNF in our experiments.

In terms of computation time, major differences were observed. The conventional methods, i.e., PCA and MNF, are non-iterative algorithms and therefore are much faster than the advanced approaches i.e., WSRRR and OTVCA which are both iterative algorithms. OTVCA performs slower than WSRRR due to the additional iteration step of the inner TV-optimization. We should note that the processing time of the advanced method could be improved using parallel programming which is out of the scope of this paper.

Applying FE and classification workflows in geological applications of spectral imaging showed to pose specific challenges which inhibit standard benchmarking approaches for accuracy assessment. Major challenges arise from partly inaccurate geological maps and limited amounts of reliable sample data. Geological maps or field sketches are often not directly transferable as validation input due to both qualitative and geolocational inaccuracies and differences in resolution. The latter are a direct consequence of the discrepancy between objective, centimeter-precise HSI data and subjectively generalized geological observations

on a decimeter to regional scale. Validation data with pixel-precision is limited to small accessible regions. These circumstances lead to either sparse or unconfident definitions of training and test pixels. We thus recommend the selection of training points based on a mixture of existing maps, geological experience and spectroscopic knowledge. We could show that by such careful selection of few, but confident training pixels, geologically sound classification results can be achieved. The returned classification accuracy figures, however, should be treated with caution, as they are often spatially unrepresentative and not an appropriate measure for the evaluation of the geological accuracy of a classified result. The challenges of the current study further show the need for well-labeled benchmark datasets for geological targets that would allow to evaluate the performance of innovative methods on a standardized, comparable basis. It also demonstrates that the rapid acquisition and processing of HS data can tremendously improve the accuracy of mapping and at the same time improve safety and decrease the time of field activities.

6. Conclusion

We applied a selection of feature extraction methods on three different data sets representing characteristic scenarios of spectral imaging in geosciences and mineral exploration. The data sets are real life case studies acquired using innovative spectral imaging approaches such as UAS-borne or small-angle terrestrial mapping and using sensors operating at different spectral ranges in the VNIR, SWIR and LWIR. To evaluate the performance of the extracted features for geoscientific applications, we subsequently applied an SVM classification using sparse training sets.

Our most important findings are:

- 1) In all three case studies, the use of machine learning algorithms allowed the discrimination of mineral domains by overall spatial and spectral differences, which is particularly advantageous for spectrally similar materials or datasets with low signal-to-noise.

- 2) Geological maps or field sketches are often not directly transferable as validation input due to generalization, local and qualitative inaccuracies, and a lack of reliable sample data. Besides the analysis of accuracy figures, additional evaluation of the classification result by geological expert knowledge is key to ensure scientifically meaningful results.
- 3) Applying FE prior to classification improved the classification accuracy and speed compared to direct classification on the whole dataset.
- 4) Innovative FE methods that promote spatial smoothness such as WSRRR and OTVCA outperformed more traditional FE methods such as PCA or MNF in all case studies. Beside the higher classification accuracy, the spatially constrained FE classification results are more accurate from a geological perspective.
- 5) While OTVCA was comparably slow, WSRRR showed the best compromise between classification accuracy and computation time of all methods. Further development and optimization of the method might allow to further speed up the processing and will be an important step towards (near-)real-time data processing.
- 6) The used methods could be successfully applied to diverse datasets in regards of spectral range, acquisition mode and data quality. The domain mapping approach using FE allowed us to extract valuable geological information even from spectrally indistinct lithologies or from data disturbed by atmospheric interference, low signal or illumination variations.

Our study promotes the use of innovative, spatially constrained FE algorithms for mineral domain mapping in geoscience and mineral exploration. The algorithms are robust against the physical content of the input dataset and can therefore be used beyond a specific type of reflectance data, for example supporting a multi-sensor classification approach.

Acknowledgment: We are grateful and thankful to the Helmholtz Institute Freiberg for Resource Technology for supporting and funding this project. We like to thank the whole department of exploration for their support during the field campaigns. We thank Jouko Jylänki and Kimmo Kärenlampi from Otanmäki Mine Oy for field support and the geologic material. The UAV HSI-VNIR data was acquired in

553 the Mulsedro project, financed by the European Union and EIT RawMaterials. The Ristonmännikkö data
554 was acquired in cooperation with the Geological Survey of Finland (GTK).

555 **Declaration of interests:** The authors declare no conflict of interest.

556 **References:**

557 Benediktsson, J.A., Ghamisi, P., 2015. Spectral-Spatial Classification of Hyperspectral Remote
558 Sensing Images, Artech House Publishers, INC, Boston, USA.

559 Chapelle, O., Vapnik, V., Bousquet, O., Mukherjee, S., 2002. Choosing multiple parameters for
560 support vector machines. Mach. Learn. 46 (1), 131–159. <https://doi.org/10.1023/a:1012450327387>

561 Fauvel, M., Tarabalka, Y., Benediktsson, J.A., Chanussot, J., Tilton, J.C., 2013. Advances in Spectral-
562 Spatial Classification of Hyperspectral Images. Proceedings of the IEEE 101 (3), 652-675.
563 <https://doi.org/10.1109/jproc.2012.2197589>

564 Ghamisi, P., Plaza, J., Chen, Y., Li, J., Plaza, A.J., 2017. Advanced Spectral Classifiers for
565 Hyperspectral Images: A review. IEEE Geoscience and Remote Sensing Magazine 5 (1), 8–32.
566 <https://doi.org/10.1109/mgrs.2016.2616418>

567 Ghamisi, P., Maggiori, E., Li, S., Souza, R., Tarablaka, Y., Moser, G., ... Benediktsson, J. A., 2018.
568 New Frontiers in Spectral-Spatial Hyperspectral Image Classification: The Latest Advances Based on
569 Mathematical Morphology, Markov Random Fields, Segmentation, Sparse Representation, and Deep
570 Learning. IEEE Geoscience and Remote Sensing Magazine, 6 (3), 10–43.
571 <https://doi.org/10.1109/mgrs.2018.2854840>

572 Green, A.A., Berman, M., Switzer, P., Craig, M.D., 1988. A transformation for ordering multispectral
573 data in terms of image quality with implications for noise removal: IEEE Transactions on Geoscience
574 and Remote Sensing 26 (1), 65–74. <https://doi.org/10.1109/36.3001>

575 Hughes, G. 1968. On the mean accuracy of statistical pattern recognizers. IEEE Transactions on
576 Information Theory 14 (1), 55–63. <https://doi.org/10.1109/tit.1968.1054102>

577 Huhma, H., Hanski, E., Kontinen, A., Vuollo, J., Mänttari I., Lahyey, J., 2018. Sm–Nd and U–Pb
578 isotope geochemistry of the Palaeoproterozoic mafic magmatism in eastern and northern Finland. Bull.
579 405 2018, 150.

580 Jackisch, R., Madriz, Y., Zimmermann, R., Pirttijärvi, M., Saartenoja, A., Heincke, B.H., Salmirinne, H.,
581 Kujasalo, J.-P., Andreani, L., Gloaguen, R., 2019. Drone-Borne Hyperspectral and Magnetic Data
582 Integration: Otanmäki Fe-Ti-V Deposit in Finland. *Remote Sens.* 11, 2084.
583 <https://doi.org/10.3390/rs11182084>

584 Jakob, S., Zimmermann, R., Gloaguen, R., 2017. The Need for Accurate Geometric and Radiometric
585 Corrections of Drone-Borne Hyperspectral Data for Mineral Exploration: MEPHySTo - A Toolbox for
586 Pre-Processing Drone-Borne Hyperspectral Data. *Remote Sens.* 2017, 9, 88.
587 <https://doi.org/10.3390/rs9010088>

588 Jia, X., Kuo, B., Crawford, M., 2013. Feature Mining for Hyperspectral Image Classification.
589 *Proceedings of the IEEE* 101 (3), 676–697. <https://doi.org/10.1109/JPROC.2012.2229082>

590 Jolliffe, I.T., 2002. *Principal Component Analysis*, Springer Series in Statistics. Springer.
591 <https://doi.org/10.1007/978-1-4757-1904-8>

592 Kärenlampi, K., Kontinen, A., Huhma, H., Hanski, E., 2019. Geology, geochronology and geochemistry
593 of the 2.05 Ga gneissic A1-type granites and related intermediate rocks in central Finland: Implication
594 for the tectonic evolution of the Karelia craton margin. *Bull. Geol. Soc. Finl.* 91, 35–73.
595 <https://doi.org/10.17741/bgsf/91.1.002>

596 Lu, D., Weng, Q., 2007. A survey of image classification methods and techniques for improving
597 classification performance. *Int. J. Remote Sens.* 28 (5), 823–870.
598 <https://doi.org/10.1080/01431160600746456>

599 Kirsch, M., Lorenz, S., Zimmermann, R., Tusa, L., Möckel, R., Hödl, P., Booyesen, R., Khodadadzadeh,
600 M., Gloaguen, R., 2018. Integration of Terrestrial and Drone-Borne Hyperspectral and
601 Photogrammetric Sensing Methods for Exploration Mapping and Mining Monitoring. *Remote Sens.* 10,
602 1366–30. <https://doi.org/10.3390/rs10091366>

603 Kirsch, M., Lorenz, S., Zimmermann, R., Andreani, L., Tusa, L., Pospiech, S., Jackisch, R.,
604 Khodadadzadeh, M., Ghamisi, P., Unger, G., Hödl, P., Gloaguen, R., Middleton, M., Sutinen, R., Ojala,
605 A., Mattila, J., Nordbäck, N., Palmu, J.-P., Tiljander, M., Ruskeeniemi, T., 2019. Hyperspectral outcrop
606 models for palaeoseismic studies. *Photogram. Rec.* 34, 385–407. <https://doi.org/10.1111/phor.12300>

607 Li, M., Zang, S., Zhang, B., Li, S., Wu, C., 2014. A Review of Remote Sensing Image Classification
608 Techniques: the Role of Spatio-contextual Information. *European Journal of Remote Sensing* 47 (1),
609 389–411. <https://doi.org/10.5721/eujrs20144723>

610 Lindholm, O., Anttonen, R., 1980. Geology of the Otanmäki mine. Häkli, T.A. (Ed.), *Proc. 26th Int.*
611 *Geol. Congr. Guid. to Excursions* 078 A+C, Part 2 (Finland), 25–33.

612 Lorenz, S., Salehi, S., Kirsch, M., Zimmermann, R., Unger, G., Vest Sørensen, E., Gloaguen, R.,
613 2018a. Radiometric correction and 3D integration of long-range ground-based hyperspectral imagery
614 for mineral exploration of vertical outcrops. *Remote Sens.* 10 (2), 176.
615 <https://doi.org/10.3390/rs10020176>

616 Lorenz, S., Kirsch, M., Zimmermann, R., Tusa, L., Möckel, R., Chamberland, M., Gloaguen, R., 2018b.
617 Long-Wave Hyperspectral Imaging for Lithological Mapping: A Case Study. *IEEE International*
618 *Geoscience and Remote Sensing Symposium (IGARSS)*, 1620–1623.
619 <https://doi.org/10.1109/igarss.2018.8519362>

620 Maier, W.D., Lahtinen, R., O'Brien, H., 2015. Mineral deposits of Finland. Elsevier, Amsterdam, The
621 Netherlands. <https://doi.org/10.1016/C2012-0-02750-0>

622 Ojala, A.E.K., Mattila, J., Ruskeenieni, T., Markovaara-Koivisto, M., Palmu, J.-P., Nordbäck, N.,
623 Lindberg, A., Aaltonen, I., Savunen, J., Sutinen, R., 2019. Postglacial Faults in Finland – a Review of
624 PGSDyn Project Results. Posiva Oy, Eurajoki, Finland. 117 pages.

625 Pääkkönen, V., 1956. Otanmäki - The Ilmenite Magnetite Ore Field in Finland. *Bull. la Commision*
626 *Geol. Finlande*, 87.

627 Pearson, K., 1901. On lines and planes of closest fit to a system of points in space. The London,
628 Edinburgh, and Dublin Philosophical Magazine and Journal of Science 2 (11), 559–572.
629 <https://doi.org/10.1080/14786440109462720>

630 Rasti, B., Sveinsson, J.R., Ulfarsson, M.O., 2014. Wavelet-Based Sparse Reduced-Rank Regression
631 for Hyperspectral Image Restoration. *IEEE Transactions on Geoscience and Remote Sensing* 52 (10),
632 6688–6698. <https://doi.org/10.1109/tgrs.2014.2301415>

633 Rasti, B., Gudmundsson, K.S., 2016. Sparse and low-rank feature extraction for the classification of
634 target's tracking capability. Proceedings of SPIE - The International Society for Optical Engineering,
635 9970. <https://doi.org/10.1117/12.2240282>

636 Rasti, B., Ulfarsson, M.O., Sveinsson, J.R., 2016. Hyperspectral Feature Extraction Using Total
637 Variation Component Analysis. IEEE Transactions on Geoscience and Remote Sensing 54 (12),
638 6976–6985. <https://doi.org/10.1109/tgrs.2016.2593463>

639 Scholkopf, B., Smola, A.J., 2002. Learning with Kernels. Cambridge, MA: MIT Press.

640 Waske, B., Benediktsson, J.A., Árnason, K., Sveinsson, J.R., 2009. Mapping of hyperspectral AVIRIS
641 data using machine-learning algorithms. Canadian J. Remote Sens. 35 (1), 106–116.
642 <https://doi.org/10.5589/m09-018>

643

644 **List of Figure Captions:**

645 *Figure 1. General workflow of hyperspectral data classification with and without prior application of*
646 *feature extraction methods*

647 *Figure 2. Location of the three study areas as well as coverage of the discussed data sets (indicated by*
648 *yellow polygons): a) UAS-based VNIR (case study 1), b) terrestrial VNIR-SWIR (case study 2), c)*
649 *terrestrial LWIR (case study 3)*

650 *Figure 3. Spectral characteristics of the classes defined for each case study area. The displayed*
651 *spectra are averages of all pixels used for training of each respective class. Spectral artefacts due to*
652 *sensor gaps and strong atmosphere-related noise are whitened out for better visibility.*

653 *Figure 4. Comparison of the six geologically most relevant feature bands per tested FE algorithm*
654 *(index indicated by number label), which were selected for subsequent classification (case study:*
655 *UAS-VNIR).*

656 *Figure 5. Performance of the tested FE algorithms in regards of processing time (in seconds per data*
657 *pixel) for the extraction of 20 image features per dataset.*

658 *Figure 6. Average performance of SVM classification in terms of accuracy using the tested FE algorithms*
659 *as well as using no prior FE*

660 *Figure 7. Performance of SVM classification based on different FE approaches for the drone-borne*
661 *VNIR survey over the Otanmäki ore deposit (Finland). A1-A5 refer to the respective class specific*
662 *accuracies.*

663 *Figure 8. Performance of SVM classification based on different FE approaches for the terrestrial VNIR-*
664 *SWIR survey at Ristonmännikö paleoseismic trenches (Finland). A1-A7 refer to the respective class*
665 *specific accuracies.*

666 *Figure 9. Performance of SVM classification based on different FE approaches for the terrestrial LWIR*
667 *survey at Naundorf quarry (Germany). A1-A7 refer to the respective class specific accuracies.*

668